JGR Space Physics

RESEARCH ARTICLE
10.1029/2018JA026397

Occurrence and Modeling Examination of Sporadic-*E* Layers in the Region of the South America (*Atlantic*) Magnetic Anomaly

Fredson Conceição-Santos[1,2], Marcio T. A. H. Muella[1], Laysa C. A. Resende[3,4], Paulo R. Fagundes[1], Vania F. Andrioli[3,4], Paulo P. Batista[3], Valdir G. Pillat[1], and Alexander J. Carrasco[5]

[1]Instituto de Pesquisa e Desenvolvimento-IP&D, Lab. de Física e Astronomia, Universidade do Vale do Paraíba-UNIVAP, São José dos Campos, Brazil, [2]Instituto Federal de Educação Ciência e Tecnologia do Maranhão-IFMA, Departamento de Extensão e Relações Institucionais, Açailândia, Brazil, [3]Divisão de Aeronomia, Instituto Nacional de Pesquisas Espaciais-INPE, São José dos Campos, Brazil, [4]State Key Laboratory of Space Weather, Chinese Academy of Science, Beijing, China, [5]Departamento de Física, Universidad de Los Andes, Mérida, Venezuela

Key Points:
- The flat/low *Es* are the most frequent types of sporadic layers observed at the low-latitude stations
- *Es* frequency parameters during moderate storms showed evidences of energetic particle-induced *E*-layer ionization around the SAMA region
- Modeled and measured electron densities revealed the role of the wind shear mechanism in the formation of the observed *Es* layers

Correspondence to:
F. Conceição-Santos,
fredcon@ifma.edu.br

Citation:
Conceição-Santos, F., Muella, M. T. A. H., Resende, L. C. A., Fagundes, P. R., Andrioli, V. F., Batista, P. P., et al. (2019). Occurrence and Modeling Examination of Sporadic-*E* Layers in the Region of the South America (*Atlantic*) Magnetic Anomaly. *Journal of Geophysical Research: Space Physics*, *124*, 9676–9694. https://doi.org/10.1029/2018JA026397

Received 12 DEC 2018
Accepted 29 OCT 2019
Accepted article online 13 NOV 2019
Published online 27 NOV 2019

Abstract In this work, the occurrence of different types of sporadic-*E* layers (*Es*) was described for two stations located in the region of the South America Magnetic Anomaly: Jataí and São José dos Campos. The results show the hourly and monthly values of the *Es* occurrences and presented five types of layers (cusp, high, flat, low, and slant), with the flat/low types ($Es_{f/l}$) being the most frequent over both stations. We also analyzed the *Es* layer parameters of blanketing frequency (f_bEs) and top frequency (f_tEs) obtained from ionosonde data during storm-time periods, in order to investigate possible evidences of energetic particle-induced *E*-layer ionization. The results revealed increases in the values of the nighttime f_tEs and f_bEs, which can be related to the particle precipitation in the South America Magnetic Anomaly region. Additionally, we investigated the roles of the wind shear mechanism in the formation of the *Es* types by using a modified form of the Ionospheric *E*-Region Model (MIRE), which incorporates tidal winds obtained from meteor radar data. Furthermore, the electron densities deduced from f_bEs parameter were compared with the maximum electron densities obtained from MIRE simulations. Depending on local time and season, the initial results revealed for both stations some discrepancies between modeled and measured electron densities. However, a better fitting was obtained when the amplitudes of the zonal/meridional wind components were adjusted by some factor, which may be attributed to the possible effects of day-to-day tidal wind variability and their interaction with gravity and planetary waves.

1. Introduction

The first observations of sporadic-*E* layers (*Es*) as evidences of an abnormal ionization at *E*-region heights were reported during the earlier 1940s (e.g., Ferrell, 1947 and references cited therein). At that time, the investigators employed radio waves reflected at the vertical incidence and point-to-point communications to monitor the spatial distribution and movement of the *Es* layers. The fading characteristics of the different *Es* echoes were important in creating the classification of the several types of sporadic-*E* layers observed from high latitudes (>60.0° in the Northern and Southern Hemispheres) to equatorial latitudes (between 5.0°N and 5.0°S). Following the primary observations, the former researchers started to hypothesize the physics behind the occurrence of *Es* layers. Among the main questions alluded by the 1940s' pioneers, one was related to the mechanisms involved in the formation of the different types of *Es* layers. The innumerable studies conducted through the approximately six decades after the first reports have in turn brought a growth in knowledge about the *Es* phenomena: (a) Auroral zone *Es* was postulated to be mainly due to charged particles penetrating into the lower ionosphere (Matsushita, 1962); (b) middle/low latitude *Es* was firstly attributed to the vertical wind shears (gradients) (Whitehead, 1961) and also due to the combined effects of ionospheric electric fields and horizontal neutral winds (Nygren et al., 1984); and (c) equatorial *Es* was considered to be a manifestation of irregularity in the equatorial electrojet (EEJ) due to the gradient E × B drift instability mechanism (Reid, 1968).

Nowadays, the advent of the newer observational techniques has provided more accurate electron density measurements at *Es* altitudes (between about 80 and 140 km) owing to the increased data resolution in

height and time. Although there is a consensus that everything about the formation of *Es* layers is not completely known, the realizations in the last 20 years of coordinated ground- and space-based experiments supported with *E*-region physics models have solved many of the questions proposed by the earlier scientists. At tropical latitudes (below 25.0° in latitude), the region of interest of this work, long-term trend studies revealed different types of *Es* layers that occurred as a manifestation of the competing roles between neutral wind shears and equatorial electric fields. For example, Abdu et al. (1996) analyzed 21 years (1975–1995) of ionosonde data at the station of Fortaleza (38.4°W; 3.9°S), Brazil, and reported a decrease in the frequency of occurrence of the equatorial type of *Es* (Es_q), while the other types of *Es* (commonly observed at low/mid latitudes) presented a systematic increase in their occurrence rates. The authors argued that the decrease in the occurrence of Es_q was mainly due to the increase in the dip latitude at Fortaleza caused by the secular variation of the geomagnetic field (northward drift of the dip equator) in the American sector. Once the Es_q layers result from irregularities in the EEJ, the increasing distance of Fortaleza from the center of the EEJ (by ~400 km) weakened the vertical polarization (Hall) electric field responsible for producing the instability process that generates the *q*-type of *Es*. The Es_q appears in the ionograms as a trace which is diffused and nonblanketing over a wide frequency range and below the maximum height of the electron density (h_mE). It is commonly observed during the daytime in the vicinity of the magnetic equator. In contrast, other types of *Es* (also known as blanketing sporadic-*E*) induced by horizontal neutral winds and wind shear mechanisms (e.g., the *l*-, *f*-, *c*-, and *h*-types) started to be observed more frequently as the dip latitude of Fortaleza changed to the edge of the latitude range covered by the EEJ. Abdu et al. (1997) also showed that the solar flux variations could modulate the occurrence rate of different types of *Es* with a maximum during the peak in the solar activity cycle. Moreover, Abdu et al. (2005) presented evidences of frequent nighttime occurrence of blanketing *Es* around the Brazilian South America (also known as South Atlantic) Magnetic Anomaly (SAMA) region, associated with a regular ionization source caused by energetic particle precipitation. Chu et al. (2014) reported a global morphological study of *Es* layer obtained from the Global Positioning System (GPS) radio occultation measurements. Their observations covered the well-known period of extreme solar minimum (2006–2011) that occurred between solar cycles 23/24. According to Chu et al. (2014), the *Es* occurrences were very rare in the geomagnetic equatorial zone (within ±3° of dip latitude), while at low-latitude regions (between 5.0° and 30.0° in the Northern and Southern hemispheres) were mainly a summer phenomenon. However, for low latitudes in the South American sector, the GPS radio occultation measurements of Arras et al. (2008) showed a somewhat higher occurrence during the autumn equinox.

Including modeling and simulation results, the most recent studies have provided relevant aspects of the physical processes that are possibly controlling the formation and disruption of the tropical *Es* layers. For example, Carrasco et al. (2007) analyzed ionosonde data and showed from model results that the *Es* occurrence at low latitudes is primarily dominated by tidal winds. However, their model also revealed that the ion convergence process for the formation of *Es* layers, primarily driven by wind shear mechanism, could be diminished after sunset due to the presence of an upward vertical electric field. The consequence of this is a disruption in the formation of *Es* layers during the evening hours associated with the prereversal zonal electric field enhancement. Otherwise, a reversal of the vertical electric field to downward could favor the formation/intensification of the *Es* layers. Yeh et al. (2014) used GPS radio occultation data and radio meteor information, with runs of the International Geomagnetic Reference Field model, Horizontal Wind Model (HWM07), and Mass Spectrometer-Incoherent Scatter model, to investigate the important role of the wind shear theory and meteor ionization mechanisms in the formation of *Es*. They argued that while the meteor ionization mechanism contributes to the source of ionized particles in the *Es* layer, the wind shear (ion convergence) mechanism explains the difference in the *Es* layer activity between the Southern and Northern Hemispheres. Fytterer et al. (2014) analyzed GPS radio occultation data to investigate the characteristics of 8-h oscillations in *Es* layer occurrence, and they found a well-pronounced peak at around 10° latitude in both hemispheres associated to the migrating terdiurnal tide. A circulation model of the atmosphere also supported the observations, and the authors concluded that the influence of terdiurnal oscillations on *Es* formation was restricted to heights above 100 km. Resende et al. (2016) employed the Ionospheric *E*-Region Model (MIRE) to investigate the competition between tidal winds and electric fields in the formation of blanketing *Es* layers. The authors showed that while the wind shear theory explains the formation of *Es* layers, the electric fields induced by the EEJ could inhibit the tidal wind effects and cause a

disruption of the blanketing *Es* at equatorial regions. More recently, Resende et al. (2017a) have incorporated wind data acquired from meteor radar observations at a low-latitude station into the MIRE model and reported a descending movement of the *Es* layers that agrees with the theory of diurnal and semidiurnal tidal effects.

With the purpose of studying the daily and monthly behavior of the different types of *Es* layers, we used the modified form of the MIRE model from Resende et al. (2017a, 2017b) to simulate the *Es* layer occurrence over two stations located in the vicinity of the SAMA region. We explore the capabilities of the MIRE model, which incorporates tidal winds inferred from all-sky meteor radar data, for firstly analyzing the correlation between the electronic densities of the *Es* layers deduced from ionograms with the electronic densities calculated by the model. Then we investigate the roles of the wind shear mechanism in the formation of the *Es* layers around the SAMA region sites. Section 2 describes the criteria for classifying the *Es* layers from the ionograms recorded by the digital ionosondes installed in the low-latitude stations of Jataí (17.9°S, 51.7° W, dip lat.: 13.4°S) and São José dos Campos (23.2°S, 45.8°W, dip lat.: 21.0°S). The basic equations of the MIRE model and the simulation procedure with the input parameters are presented in section 3. The methodology to infer the neutral winds is briefly described in section 4. The results and discussions are given in section 5, followed by the conclusions.

2. Sporadic-*E* Layer Parameters From Ionosonde Data

The study described in this work is based on sporadic-*E* layer (*Es*) data obtained from two digital ionosondes: one located in Jataí and another in São José dos Campos. The observatories of Jataí (hereafter referred to as JAT) and São José dos Campos (hereafter referred to as SJC) are located at longitudes of the SAMA region, where the geomagnetic total field intensity is unusually low. For example, Figure 1 shows the configuration of the total magnetic field intensity distribution over the globe, in which its lowest value over South America indicates the position of the center of the SAMA. It can also be noticed from Figure 1 that the center of the SAMA region is located somewhat between Southern Brazil and Northern Argentina, the reason the scientific community is naming SAMA as now South America Magnetic Anomaly instead of South Atlantic Magnetic Anomaly. The boundary between Brazil and Argentina is highlighted in this figure through the dotted black line. The red dots indicate the location of the observatories of JAT and SJC.

The ionosonde data were collected during the months of April, June, September, and December of the year 2016. The ionosondes used in this work are of the type CADI (Canadian Advanced Digital Ionosonde). The CADI ionosondes operate using a double delta antenna for both transmitting and receiving. The transmitter used by the CADI system scans frequencies from 1 to 20 MHz with a power of 600 W. It sweeps with a pulse width of 40 μs, which gives ±3 km height resolution (MacDougall et al., 1995). The *Es* layer data were scaled using the software tool named UDIDA-UNIVAP Digital Ionosonde Data Analysis (Pillat et al., 2013), which facilitates the visualization of the ionograms on a PC screen. In this work, the virtual height (*h*′Es) and blanketing frequency (*fb*Es) parameters were scaled from the ionograms recorded every 5 min at JAT and SJC, totaling about 8,640 ionograms per month. Then the type of the *Es* layers registered on the ionograms was classified according to the criterion established by the Union of Radio Science. These classifications are available in the U.R.S.I. Handbook of Ionogram Interpretation and Reduction (Piggott & Rawer, 1972). During the analyzed period, it was possible to identify five distinct types of *Es* layers in the ionograms recorded by the ionosondes of JAT and SJC. Examples of the ionograms showing the signatures of these five types of *Es* layers are shown ahead in Figure 2. These types of *Es* layers are defined as cusp (Es_c), high (Es_h), flat (Es_f), low (Es_l), and slant (Es_s).

According to Piggott and Rawer (1972), the cusp type (Es_c) can be interpreted as a trace that shows a cusp relatively symmetrical in the critical frequency of the *E* layer (f_oE) or below it. This type of *Es* layer commonly appears during daytime embedded between the bottom of the *E* layer and the maximum height of the electron density (h_mE). The sporadic-*E* layer classified as high is represented by "Es_h." This type is commonly observed during daytime and is interpreted in the ionograms as a trace that shows a discontinuity in height with the trace of the normal *E* layer at the critical frequency (f_oE) or above it. A cusp is also observed, but it seems asymmetric, and the low frequency end of the *Es* trace is clearly located above the high frequency end of the normal *E* trace. The flat type (Es_f) of the sporadic layer occurs during nighttime and refers to a relatively solid trace that shows no appreciable increase in height with frequency. The classification of

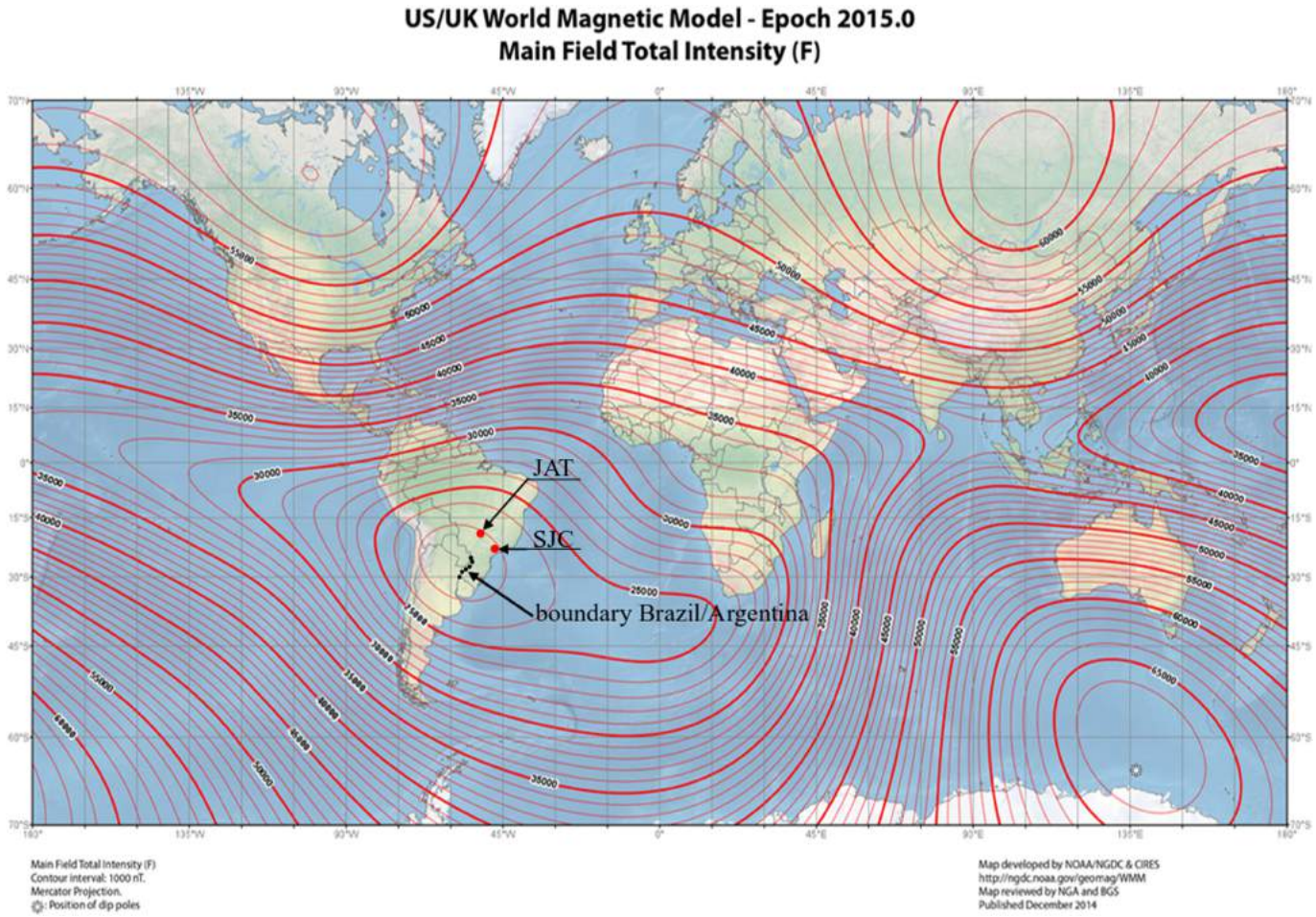

Figure 1. Isolines of the geomagnetic field total intensity distribution over the globe in which its lowest values over South America defines the present region of the South America (former Atlantic) Magnetic Anomaly.

this type can only be used when a thick *E* layer is generally not observable (or when a numeric value of frequency parameter f_oE cannot be obtained).

The low type (Es_l) of the sporadic layer is defined as a flat trace, which manifests during daytime below the minimum virtual height of the normal *E* layer (h_mE). However, since the "Es_f" and "Es_l" types have practically the same profile, varying only with the time of manifestation, their occurrence was grouped into one and named "$Es_{f/l}$." The last type of sporadic layer also identified in the ionograms is named slant (Es_s). This sporadic layer is defined as a diffuse trace that grows continuously with frequency and usually emerges from another type of *Es* trace. Also according to Piggott and Rawer (1972), the slant trace may arise from f_oE, f_xE, f_oEs, f_xEs, or another intermediary point in the associated trace. It is well known that all these types of *Es* layers mentioned above are formed by vertical shear in the horizontal winds, which are driven by tidal motions and/or gravity waves (Cohen et al., 1962; Resende et al., 2013; Whitehead, 1989).

3. MIRE Model

We used the MIRE originally developed by Carrasco (2005) and Carrasco et al. (2007), which was modified by Resende et al. (2017a, 2017b). The extended version of MIRE included two major modifications: (1) Inclusion of a new wind model that correctly describes the wind dynamic over the Brazilian region; and (2) the seasonal variability of the metallic ions in the *Es* layer formation. MIRE model allows to build a profile of the electronic density at heights of the *E* region and, thereby, to identify the presence of a sporadic-*E* layer by using the equation of continuity to calculate the sum of the ionic density for the main constituents,

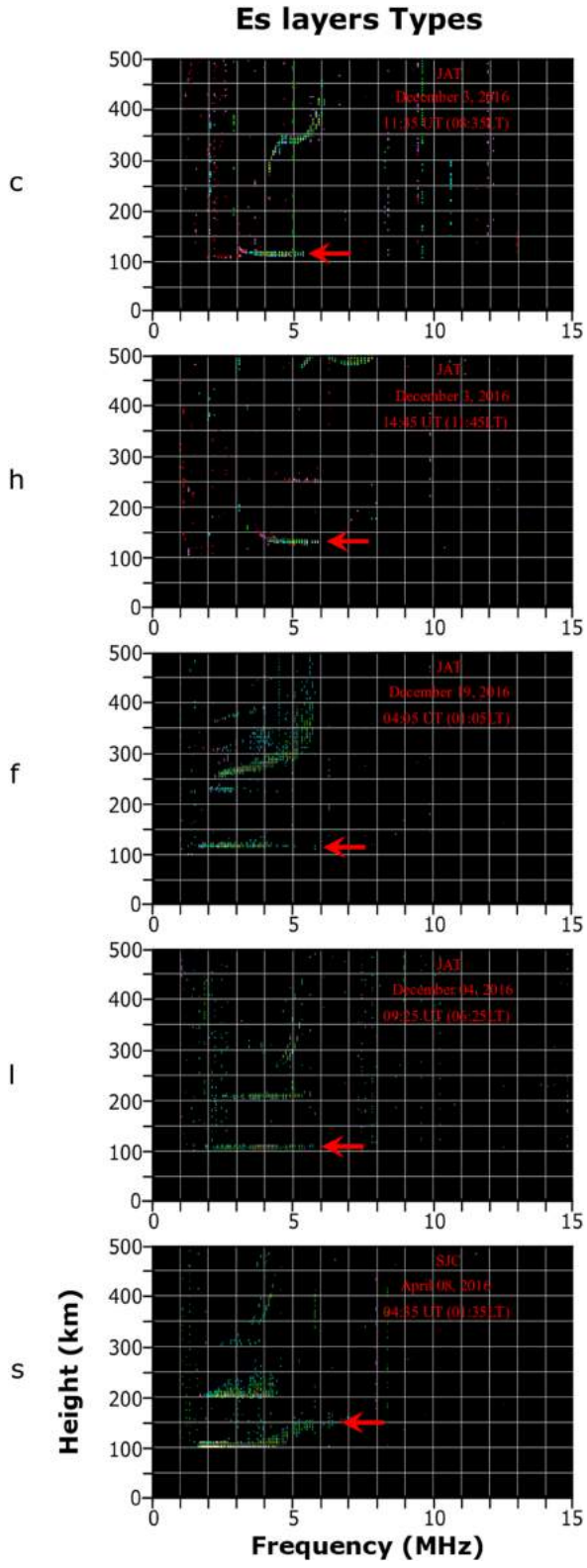

Figure 2. Ionograms identifying the five types of layers that were observed in JAT and SJC in the months of April, June, September, and December of 2016. From top to bottom are shown examples of the Es_c, Es_h, Es_f, Es_l, and Es_s types of *Es* layers. The red arrows indicate the traces of the sporadic layers in the ionograms.

such as NO^+, O_2^+, O^+, N_2^+, Fe^+, and Mg^+. The metallic ions (Fe^+ and Mg^+) were used since they are more significant in the formation of the *Es* layers (Helmer et al., 1998).

It is well known that the ionic density profile in the ionosphere is formed through the transport and chemical processes. In terms of transport, although the existing horizontal movements diffuse quite rapidly, they do not contribute significantly to the transport term $\nabla.(V_i[N_i])$ since the horizontal gradients of N_i and V_i are generally much smaller than the vertical gradients (Rishbeth & Gariott, 1969). Thus, considering only the vertical direction, the equation of continuity that takes into account the temporal variation of each constituent is given in MIRE model by the following general equation:

$$\frac{\partial[N_i]}{\partial t} = P - L - \frac{\partial(V_{iz}[N_i])}{\partial z}, \quad (1)$$

where $[N_i]$ is the numerical density of each ion species, P is the production rate per unit volume, L is the loss rate per unit volume, V_{iz} is the velocity of the ions in the vertical direction, and the product $(V_{iz}[N_i])$ denotes the dynamics of ions' flux. The production (P) and the loss (L) terms are related to chemical processes.

MIRE model calculates the electronic density in a range spanning from 86 to 140 km by using for each of the ion species the continuity for metallic (Fe^+ and Mg^+) and molecular ions (NO^+, O_2^+, O^+, and N_2^+), as shown in Carrasco et al. (2007) and Resende et al. (2017a). It is important to mention that between the heights of 90 and 150 km, the loss rate of N_2^+ and O^+ ions when converted to O_2^+ and NO^+ is practically equal to the rate of production by photoionization. Therefore, the transport term is neglected for these ions. However, for the other four constituents, one has to consider the transport term that is given by the following equation:

$$V_{iz} = \frac{\omega_i^2}{(\nu_{in}^2 + \omega_i^2)}\left[\cos I \cdot \sin I \cdot U_x + \frac{\nu_{in}}{\omega_i}\cdot\cos I \cdot U_y + \frac{1}{\nu_{in}}\frac{e}{m_i}\cdot\cos I \cdot \sin I \cdot E_x\right. \quad (2)$$
$$\left. + \frac{e}{\omega_i m_i}\cdot\cos I \cdot E_y + \frac{e}{\nu_{in} m_i}\cdot\left(\frac{\nu_{in}^2}{\omega_i^2} + \sin^2 I\right)\cdot E_z\right],$$

where ω_i is the gyrofrequency, ν_{in} is the ion-neutral collision frequency, the indexes i and n refer to the ions and neutrals, respectively, I is the magnetic inclination angle, m_i is the mass of the ion, e is the electric charge of the ion, E_x,E_y, and E_z represent the components of the electric field, and U_x and U_y denote the meridional (southward) and zonal (eastward) components of the neutral winds, respectively. The contribution of the electric fields in the formation of the *Es* layers at low-latitude regions is negligible when compared to the controlling effects of the neutral winds (Dagar et al., 1977). In this work, since we analyzed data from two low-latitude stations and no occurrence of the equatorial type of *Es* (Es_q) was registered in the ionograms, only neutral wind measurements were considered as input to the MIRE model.

A complete outlining of the main equations that describe the MIRE model can be found in the works of Carrasco et al. (2007) and Resende et al. (2017a), and therefore, the full mathematical description will not be repeated here. However, it is important to mention that the MIRE

model uses the Crank-Nicolson method to calculate the equations, which consists of discretizing the domain in points (t_i and z_j). The set of these points will define the mesh (2,401 × 1,081 points), which in this case is two-dimensional with spacing $\Delta z = 0.02$ km for the height and a time step $\Delta t = 5$ minutes for the temporal discretization. The Crank-Nicolson method implements the approximations of differences at the midpoint of the time increment. Finally, after calculating the density of each ion constituent, we obtain the electronic density $[n_e]$ as given by:

$$[n_e] = \left[O_2^+\right] + [NO^+] + [O^+] + \left[N_2^+\right] + [Fe^+] + [Mg^+]. \quad (3)$$

4. Meteor Radar Wind Data

In this work, we used observational data collected by the All-Sky Interferometric Meteor Radar (SKiYMET) installed in the low-latitude station of Cachoeira Paulista (22.7°S, 45.0°W, dip lat. 21.1°S) to infer the winds and atmospheric tides in the height ranging between 80 and 100 km. The SKiYMET monitors the drift of the meteor trails by using interferometric and Doppler techniques to determine the position and radial velocity of the meteor echoes. According to Batista et al. (2004), for each signal echoed by the meteoric trails, the radial velocity is determined, and the height and azimuth are localized by the correlation between the signals captured by the receiving antennas and the delay of the pulses. According to Hocking et al. (2001), the SKiYMET radar rejects entirely the radial velocities with the standard deviation for the mean greater than 5.5 ms^{-1} (used by the system as an estimate for the error). Then the mean meridional and zonal winds are computed by separating the echoes in height/time bins. Therefore, we extracted the parameters of the diurnal and semidiurnal tides, as well as the wind amplitudes, wavelengths, and phases. A more detailed description about the radar system installed at Cachoeira Paulista and the methodology used to compute the neutral wind parameters and the uncertainties associated can be found in the previous works of Hocking and Thayaparan (1997), Hocking et al. (2001), Batista et al. (2004), and Andrioli et al. (2009, 2013).

As mentioned before, only neutral wind parameters have been considered as input to the *E*-region model in order to examine the *Es* layer formation over the stations of JAT and SJC. The parameters obtained from the observational meteor radar wind data at Cachoeira Paulista were included in the following equations (Mathews & Bekeny, 1979):

$$U_x(z) = U_{x0}(z)\cdot\cos\left(\frac{2\pi}{\lambda_x}(z-z_0) + \frac{2\pi}{T}(t-t_{x0}(z))\right), \quad (4)$$

$$U_y(z) = -U_{y0}(z)\cdot\sin\left(\frac{2\pi}{\lambda_y}(z-z_0) + \frac{2\pi}{T}(t-t_{y0}(z))\right), \quad (5)$$

where $U_{x0}(z)$ and $U_{y0}(z)$ correspond to wind amplitudes at the height z; λ_x,and λ_y denote the wavelengths; T is the period of the tide (24 h for diurnal and 12 h for semidiurnal); z_0 is a reference height assumed as being 100 km; and $t_{x0}(z)$ and $t_{y0}(z)$ are the wave phases.

The measurements available from the meteor radar provide data from 80 to 100 km. However, the range of height of interest in MIRE to simulate the *E* region and the *Es* layer dynamics is from 86 to 140 km. Thus, in order to extend the wind equations up to 140 km, we proposed fitting functions for each parameter. A detailed description of the methodology used to compute the wind parameters for altitudes above 100 km is available in Resende et al. (2017a, 2017b). However, we performed some modifications in MIRE to obtain a more realistic wind profile. In fact, Resende et al. (2017a, 2017b) considered a constant wavelength in their simulations. Here, we adjust a wavelength tending to infinity above 120 km. This choice was based on the results reported by Lieberman et al. (2013). They have shown that the tidal wind has a wavelength that is not constant in height. The authors analyzed the migrating and nonmigrating diurnal tides between 90 and 270 km from data collected by the wind imaging interferometer onboard the Upper Atmosphere Research Satellite. Our extrapolation results agreed in amplitude and phase with the observations reported in the work of Lieberman et al. (2013).

Finally, the wind measurements from Cachoeira Paulista were used in this study as representative of the winds over JAT and SJC since no other measurements at any low-latitude station were available

simultaneously with the ionosonde observations. Thus, the inferred neutral wind components were included in equation (2) of MIRE model to simulate the *Es* layer dynamics over the two observatories.

5. Results and Discussions

5.1. Daily and Monthly Distribution of the *Es* Layers

Figure 3 shows the hourly percentage occurrences of the "*s*," "*h*," "*c*," and "*f/l*" types of *Es* layers for the months of September, December, April, and June of the year 2016 over the stations of JAT and SJC. The percentage of occurrence shown in Figure 3 was computed by the ratio between the hourly observations of each type of sporadic layers, with respect to the total number of sounding measurements recorded in each specific hour during the entire month. Figure 3 reveals that in general, a higher frequency of occurrence of the type $Es_{f/l}$ is observed for all months and over both stations. Then it is followed by the Es_c and Es_h types. The Es_s type of sporadic layer seems to be less frequent over the two stations. The green lines in the plots of Figure 3 show the *Es* occurrence rates for each month. It is possible to see that over SJC (panels in the right column), the occurrence of *Es* is higher during April with 31.76%, followed by December (28.20%), June (22.20%), and September (17.84%). An almost similar diurnal pattern has been observed further north at the station of JAT (panels in the left column), with the average occurrence of *Es* attaining 32.56% in April. Nevertheless, the *Es* layer occurrence seems to be higher in June (27.92%) than in December (22.14%), with the month of September also being the less frequent in *Es* occurrence (17.38%) as observed at SJC. The higher occurrence rates of *Es* layers observed during April for the longitude of the two stations analyzed here are consistent with the previous results reported by Arras et al. (2008), when using radio occultation measurements from different satellites showed the global distribution of *Es* seasonal occurrence. The statistical results from Figure 3 also show that, differently from middle latitudes where the *Es* layer events are more expressive during summer (as in the month of December), over the Brazilian low-latitude stations of SJC and JAT, the *Es* occurrence seems to be maximum in April (typically an equinoctial month). It is worthwhile mentioning that the overall occurrence of sporadic layers considering all days of the 4 months (results not shown in the plots of Figure 3) was 24.86% and 28.90% in SJC and JAT, respectively.

A more detailed inspection of the plots shown in Figure 3 reveals that the Es_s type is rarely observed during September and December over both JAT and SJC. In these months, the Es_s type occurs after midnight until before sunrise, and its observation is limited to a couple of minutes within 1 hour of sounding. Although the Es_s percentage of occurrence during April over JAT (with ~0.3-1.4%) and SJC (with ~0.8-3.6%) is still negligible compared to other types, it starts to be observed just around sunset and ends at presunrise hours. In June, a maximum of 5% is observed over JAT, but the beginning of the Es_s type was displaced to afternoon (at around 15:00 local time (LT)), and its occurrence restricted to premidnight hours. Over SJC in June, the Es_s type occurrence is also restricted to premidnight hours, but it starts around sunset as in the month of April and attains a maximum of ~3.9%. The slant type of sporadic layer (Es_s) observed here is characterized by the oblique propagation of the radio signal. According to Cohen et al. (1962), it may be associated with the presence of irregularities embedded in the *E* layer or due to different tidal winds configuration. In general, the Es_s type is observed in the equatorial region. However, the cases of slant sporadic found in our analysis over the low-latitude stations of JAT and SJC strongly suggest that tidal winds are dominating the generation of this type of *Es* layer.

The *h*-type of sporadic *E* (Es_h) is known to be developed around 130–150 km. The sequence of ionograms analyzed for JAT and SJC showed that the Es_h type tends to present a descending movement in the ionosphere until to become an Es_c type around ~105–120 km. This is a well-known behavior already reported in previous studies (e.g., Abdu et al., 1997; MacDougall, 1974). The occurrence of both Es_h and Es_c types is larger over JAT than over SJC for all months. In addition, an overall analysis also shows that the occurrence of the Es_c type tends to dominate in relation to the Es_h type. Except for September over SJC, during all other months over both stations, the occurrences of the Es_h and Es_c get dominant and prevail against other types of *Es* between around 10:00 and 16:00 LT. It is possible to see from Figure 3 that the frequency of occurrence of the Es_h and Es_c types is comparatively lower during September. For example, over JAT during September, the Es_h occurrence peaks between 10:00 and 12:00 LT (~13.6–16.9%), whereas the Es_c type peaks around 16:00–18:00 LT (~18.3–19.7%). On the other hand, over the station of SJC, their occurrences during September can be considered negligible (~0.3–3.6%). In the months of December and April over both JAT

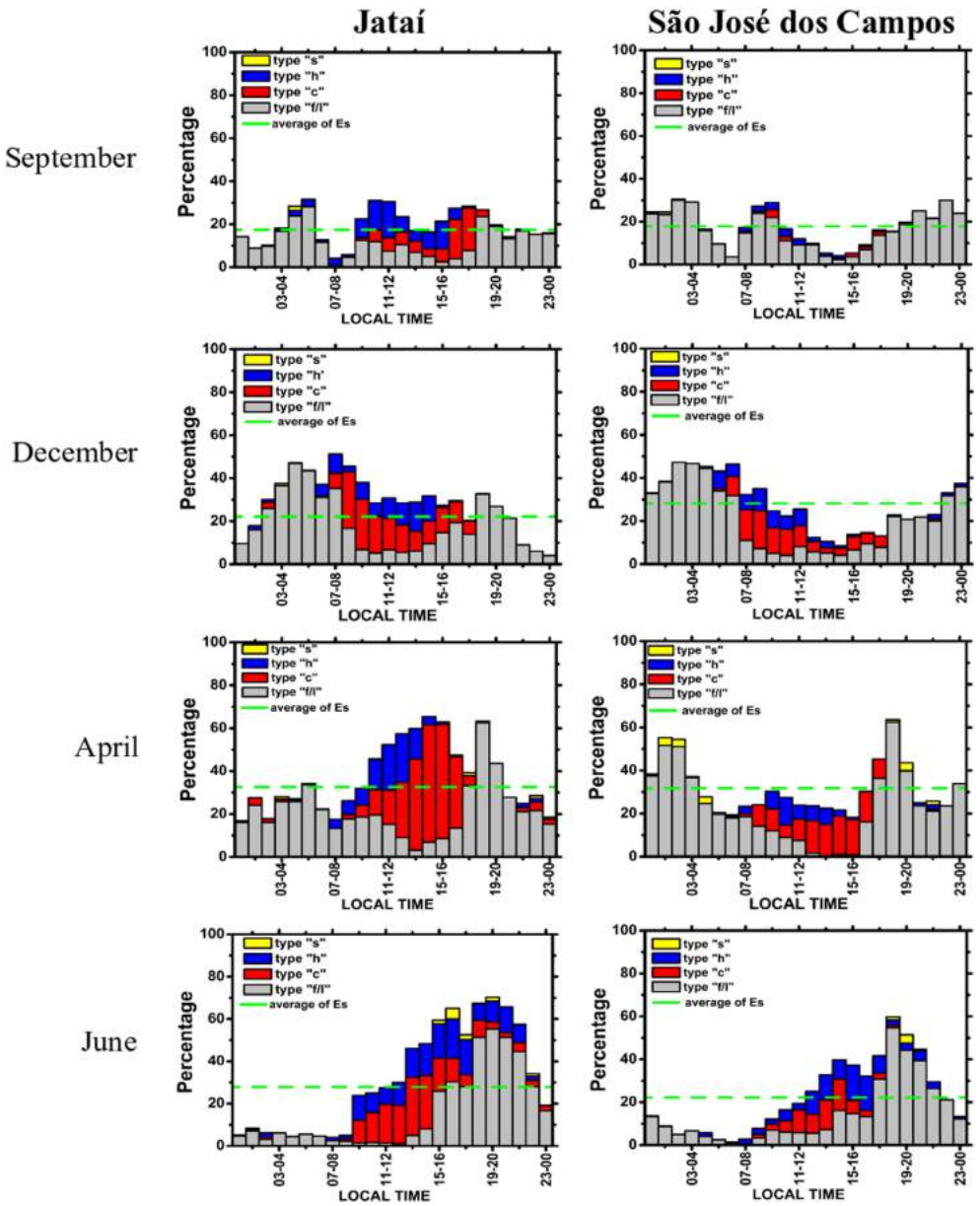

Figure 3. Hourly and monthly values of percentage occurrence of the "Es_s," "Es_h," "Es_c," and "$Es_{f/l}$" types of sporadic layers at JAT (left panels) and SJC (right panels).

and SJC, the Es_h and Es_c occurrences are almost absent during nighttime, but it is clearly noticed that there is an enhancement after sunrise. A maximum Es_h occurrence of ~10.3–13.5% is observed between around 12:00 and 15:00 LT during December over JAT, while over SJC, a maximum is not well defined, but it seems to occur during morning hours. During April, a maximum Es_h occurrence of ~22.6% is observed over JAT around noon and ~12.8% between around 10:00 and 11:00 LT over SJC. In the case for the month of June, its occurrence over JAT increases steadily after sunrise and reaches maximum values of ~18.6% between around 13:00 and 17:00 LT. It persists during the first evening hours and starts to decrease after 22:00 LT. For SJC, it shows a slight increase (up to ~16.4%) until around 15:00–17:00 LT, when its occurrence begins to decrease until negligibly small values after 22:00 LT. In terms of the Es_c type, its frequency of occurrence is higher during April over JAT than in the other months, including those analyzed for the station of SJC. It rises sharply after sunrise and reaches the highest values of ~42.5–54.6% between around 13:00 and 16:00 LT. At around the same time during June, a maximum Es_c occurrence of ~27.5% is

observed over JAT. Otherwise, during December, the amplitude of this maximum (~26.3%) occurs in the morning. An important aspect also noticed from Figure 3 is the fact that the Es_c type occurrence over SJC for all months is mostly restricted to sunlit hours. Its maximum value is observed in the morning during December (~17.5% at around 08:00–09:00 LT) and in the afternoon during April (~17.8% at around 14:00–15:00 LT) and June (~14.7% at around 14:00–15:00 LT).

The $Es_{f/l}$ is a typical type of sporadic layer that occurs generally in the height ranging from 100 to 105 km. As mentioned before, the $Es_{f/l}$ type is the most frequent throughout the months analyzed for both stations. The $Es_{f/l}$ occurrence is also higher during nighttime than during the daytime; a typical feature also reported by Abdu et al. (1996, 1997) over the station of Fortaleza (38°W, 4°S), Brazil. The $Es_{f/l}$ type showed significant increase in the occurrence during postmidnight hours in December (maximum percentage of ~47.2%) and during premidnight hours in June (maximum percentage of ~55.3%) over both JAT and SJC. A secondary peak of ~32.6% was observed in December over JAT at around 18:00–19:00 LT. For the months of April and September, the occurrence rates of the $Es_{f/l}$ type are noticeably lower than during the months of June and December, in which the higher values were obtained during April, with a peak of ~62.5% at around 18:00–19:00 LT over JAT and two peaks at around 01:00–03:00 LT (~51.7%) and 18:00–19:00 LT (~62.5%) over SJC.

5.2. *Es* Layer Characteristics in the SAMA During a Case of Magnetically Disturbed Condition

The *Es* layer occurrences over JAT and SJC obtained during both geomagnetically quiet and disturbed days were not separated and were grouped into the same statistical results presented in Figure 3. This separation was not performed due to the absence in the ionograms of any type of *Es* layer associated with significant precipitation of energetic particles. As the observatories of JAT and SJC are located inside the region under the effects of the SAMA, it would be expected a regular source of ionization in the *E* region over these stations associated with particle precipitation. For example, Abdu et al. (2005) presented strong evidence of energetic particle-induced *E*-layer ionization at the Brazilian SAMA region even during geomagnetically quiet periods. Moreover, according to Batista and Abdu (1977), under magnetospherically disturbed conditions the occurrence, as well as the intensity of the *Es* layers, can be significantly enhanced in the SAMA longitude sector. Furthermore, owing to the weakness of the geomagnetic field at the SAMA and the associated enhanced particle precipitation, a different type of *Es* layer, which is typical of auroral regions, could also be identified in the ionograms. This type of sporadic layer is known as auroral (Es_a) and is manifested by traces of range spreading (hundreds of km) of *Es* echoes. In the work of Batista and Abdu (1977), they observed over the low-latitude station of Cachoeira Paulista, Brazil, the occurrence of Es_a layers during the recovery phase of a geomagnetic storm. More recently, Resende et al. (2013) also reported during the recovery phase of a very intense geomagnetic storm the presence of Es_a layers but for a station located in the Brazilian equatorial region (São Luís: 2.33°S; 44.21°W; dip angle: −4.5°). In the present study, the signatures of the Es_a type of sporadic were not observed in the ionograms recorded at JAT and SJC, which suggests that the influence of the SAMA was not significant over these stations. The absence of the Es_a type of sporadic can be first attributed to the fact that intense/very intense geomagnetic storms did not occur during the periods analyzed in this study. Moreover, based on the studies presented by previous authors, it seems that the occurrence of Es_a layers may depend on the location of the center region of maximum particle flux. Although the stations of JAT and SJC are located inside the region influenced by the SAMA, with the westward secular drift of the geomagnetic anomaly, the center region has possibly moved well into the Argentine region, which can explain the absence of the Es_a layers in our observations.

However, during the 4 months analyzed in this work, it was possible to observe evidence of energetic particle-induced *E*-layer ionization around the SAMA region associated with enhanced geomagnetic activity. Although Es_a layers have not been detected over JAT and SJC, during some events of a moderate geomagnetic storm, the ionograms revealed increases in the *Es* layer frequencies, such as in the f_bEs (the blanketing frequency) and the f_tEs (the top frequency) parameters. For example, in Figure 4, we show the *Es* layer frequency parameters and the geomagnetic Kp and Dst indexes recorded during the moderately disturbed period of 1–5 September 2016. In the panels of Figure 4 is shown (from top to bottom) the f_tEs reflected by the sporadic layers over JAT and SJC, then the plasma frequency indicated by the f_bEs over JAT and SJC, and in the bottom panel the values of the Dst/Kp indexes. In the f_tEs and f_bEs plots, the gray

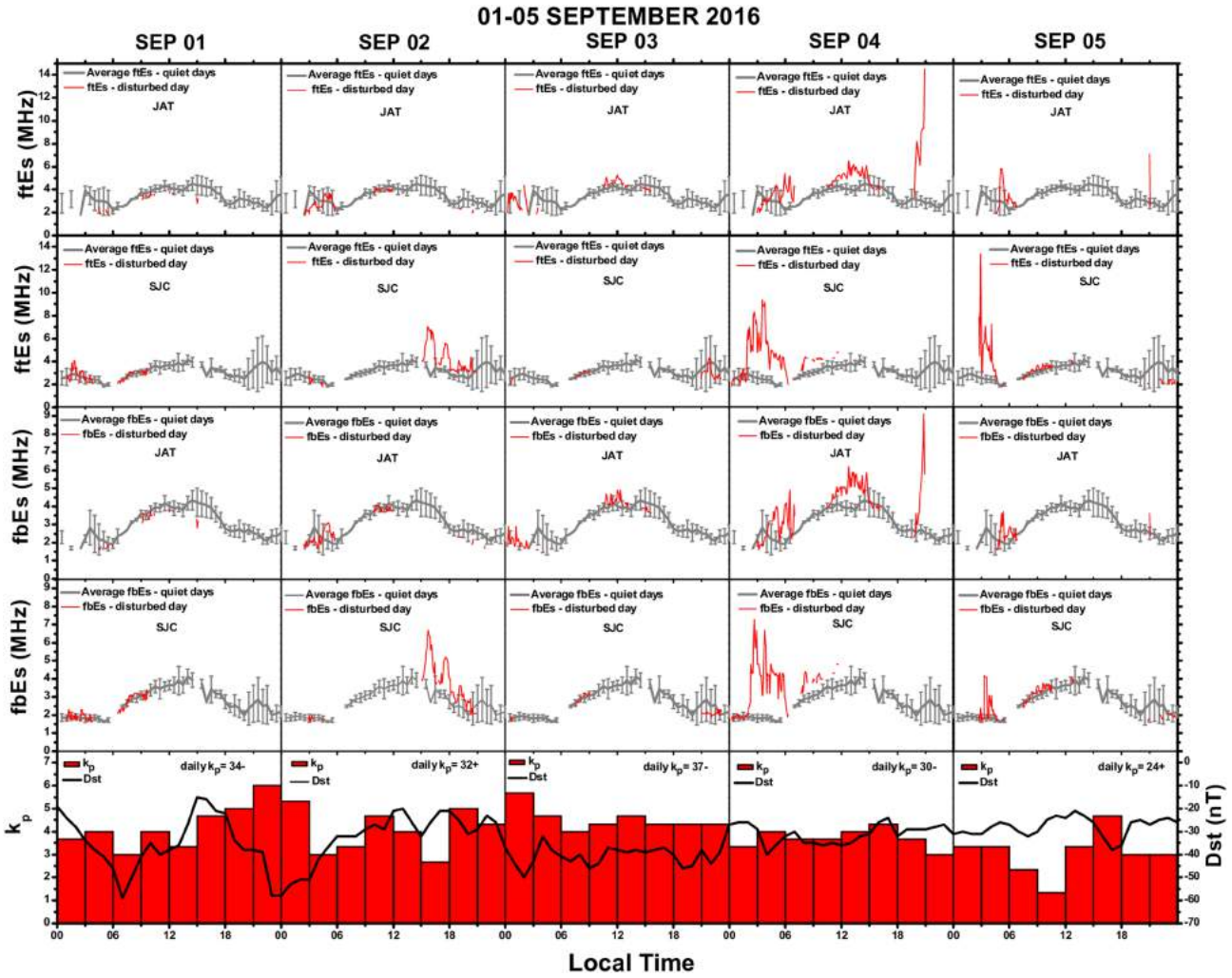

Figure 4. The two top panels show the mean quiet-time (gray lines) and storm-time (red lines) values of the top frequency (f_tEs) reflected by the sporadic layers at JAT and SJC, respectively, during the moderately disturbed period of 1–5 September 2016. Similarly, in the middle panels is shown the blanketing frequency (f_bEs) at JAT and SJC. The Kp and Dst values are shown in the bottom panel.

lines indicate the daily mean values during the geomagnetic quiet days (ΣKp < 24), and the error bars represent a standard deviation, while the red lines indicate the values during the disturbed days. The geomagnetic indexes reveal that the period from 1 to 3 of September was the most disturbed with the 3-hourly planetary Kp index (daily) ranging from 32^+ to 37^- and attaining a maximum value of 6^0 between 21:00 and 24:00 LT on 1 September. The storm's sudden commencement occurred on 31 October (not shown in the plots) and occasioned the horizontal component of the Earth's magnetic field to attain a maximum negative Dst index value (solid line) of about −60 nT at around 07:00 LT on 1 September. Then it was followed by other compressions that led the intensities of Dst to attain about −58 nT between around 23:00 and 24:00 LT on 1 September and about −50 nT at ~02:00 LT on 3 September.

An anomalous intensification of f_tEs and f_bEs accompanied by oscillatory values of their intensity can be noted in the plots of SJC between around 15:00 and 21:00 LT on 2 September. These intensifications of the frequency parameters (maximum of ~6.8 MHz) reveal increases in the *Es*-layer ionization over SJC, which might have some contribution associated with particle precipitation (mainly during nighttime). During the recovery phase of the storm on 4 and 5 September, again the results revealed strong fluctuations of f_tEs (maximum of ~13.4 MHz) and f_bEs (maximum of ~7.3 MHz) over SJC but now during postmidnight hours from around 02:00 LT until near sunrise. Around the same time, the intensification of the *Es* layer density (determined from f_tEs and f_bEs) was also observed simultaneously over JAT but with maximum

frequencies attaining comparatively lower values (of ~5 MHz). Over JAT, enhanced *Es*-layer ionization was also observed around noon on 4 September and then an anomalous peak at ~20:00 LT. Batista and Abdu (1977) and Abdu et al. (1981) reported during the recovery phase of magnetic storms, electron density enhancements over Cachoeira Paulista associated with particle precipitation. They presented evidence that such particle precipitation from the Van Allen radiation belt might be an important source of enhanced ionization during nighttime. However, they identified that associated with the f_tEs and f_bEs enhancements, Es_a type of sporadic layers has occurred. It is worthwhile mentioning that the studies conducted by Batista and Abdu (1977) and Abdu et al. (1981) were carried out in the station of Cachoeira Paulista (CXP), which is close to the station of SJC by ~100 km. However, at that time, the station of CXP was well located under the center of the geomagnetic anomaly. Although the results revealed by the previous works show us that we cannot totally exclude the possibility of additional ionization source due to precipitation of charged particles, the absence of Es_a layers in our observations suggests that the enhancements of the *Es* electron densities are associated with redistribution of ionization driven by the wind shear mechanism. The role of the neutral winds in the formation of the *Es* layers in the SAMA region over the stations of JAT and SJC is discussed ahead in section 5.3.

5.3. Neutral Wind Calculation and *E*-Region Simulations

This section presents the results on the amplitude of the meridional and zonal wind components computed from observations of the meteor radar installed at Cachoeira Paulista. These are the measured values of neutral wind used as input in MIRE to provide the simulations of the *Es* layers over JAT and SJC. Then, the vertical profiles of the *E*-region electron density are simulated over both the stations along the different months. Finally, a comparison between the observed and simulated maximum electron densities is presented and discussed.

5.3.1. Neutral Wind Profiles

As mentioned in section 4, the MIRE model is employed here to simulate the *Es* layers over JAT and SJC by using the neutral wind model inferred from the SKiYMET meteor radar data collected at Cachoeira Paulista. Figure 5 shows the height-time maps of wind amplitudes over Cachoeira Paulista computed from the fitted model for the meridional and zonal components. The format of the maps is represented in the height versus LT scheme, and the colored bars indicate the wind component amplitudes. In all profiles for the months of September, December, April, and June are noticed the heights with amplitude values equal to zero, which reveal the presence of wind shearing that explains the mechanism of formation of the *Es* layers. We found that the behavior of the meridional and zonal neutral winds observed here for the station of Cachoeira Paulista is in good agreement with the previous results reported by Batista et al. (2004).

It is observed in Figure 5 that in general, the amplitudes of the zonal wind component (positive eastward) are higher than those observed for the meridional wind (positive northward). The amplitudes of the zonal wind are larger in the months of December and April (between around −70 and 70 ms^{-1}) and lower in September (−28-25 ms^{-1}), whereas for the meridional component, the amplitude is comparatively larger in December (between around−20 and 24 ms^{-1}) and also lower in September (between around−6.0 and 5.5 ms^{-1}). In addition, the results in Figure 5 also reveal that the wind profile for the zonal and meridional components seems to have a more irregular behavior in December than in the other months, whereas in June, the wind shear is steadier.

5.3.2. Comparison Between Modeled and Measured *Es* Electron Densities

Figure 6 shows the electron density (in electrons/cm^3) simulated by MIRE considering in the model as input the neutral wind profiles described in the previous section (Figure 5). As an example, in the plots of Figure 6 was considered a case during the month of June. The figure shows the evolution of *Es* layers (electron density log-scale profile) in relation to height for three different moments (at 00:00 LT, 09:00 LT, and 16:00 LT). The peaks in the electron density profile characterize the presence of *Es* layers, which are indicated in the plots by the red arrows. At 00:00 LT it is possible to observe from Fig. 6 the formation of two *Es* layers, one at ~104 km and another at ~123 km. In the morning at 09:00 LT, two *Es* layers are observed simultaneously at ~109 km and 127 km, whereas at 16:00 LT, only one layer is observed at around 116 km height. The simulation results also show that the maximum density at *Es* layer heights during nighttime (00:00 LT) was ~$10^{4.5}$ electrons/cm^3, whereas during daytime was ~$10^{5.5}$ electrons/cm^3. A relevant feature inspected by the simulation results shows the nighttime *Es* layers evolving and decreasing with height. For example, the highest

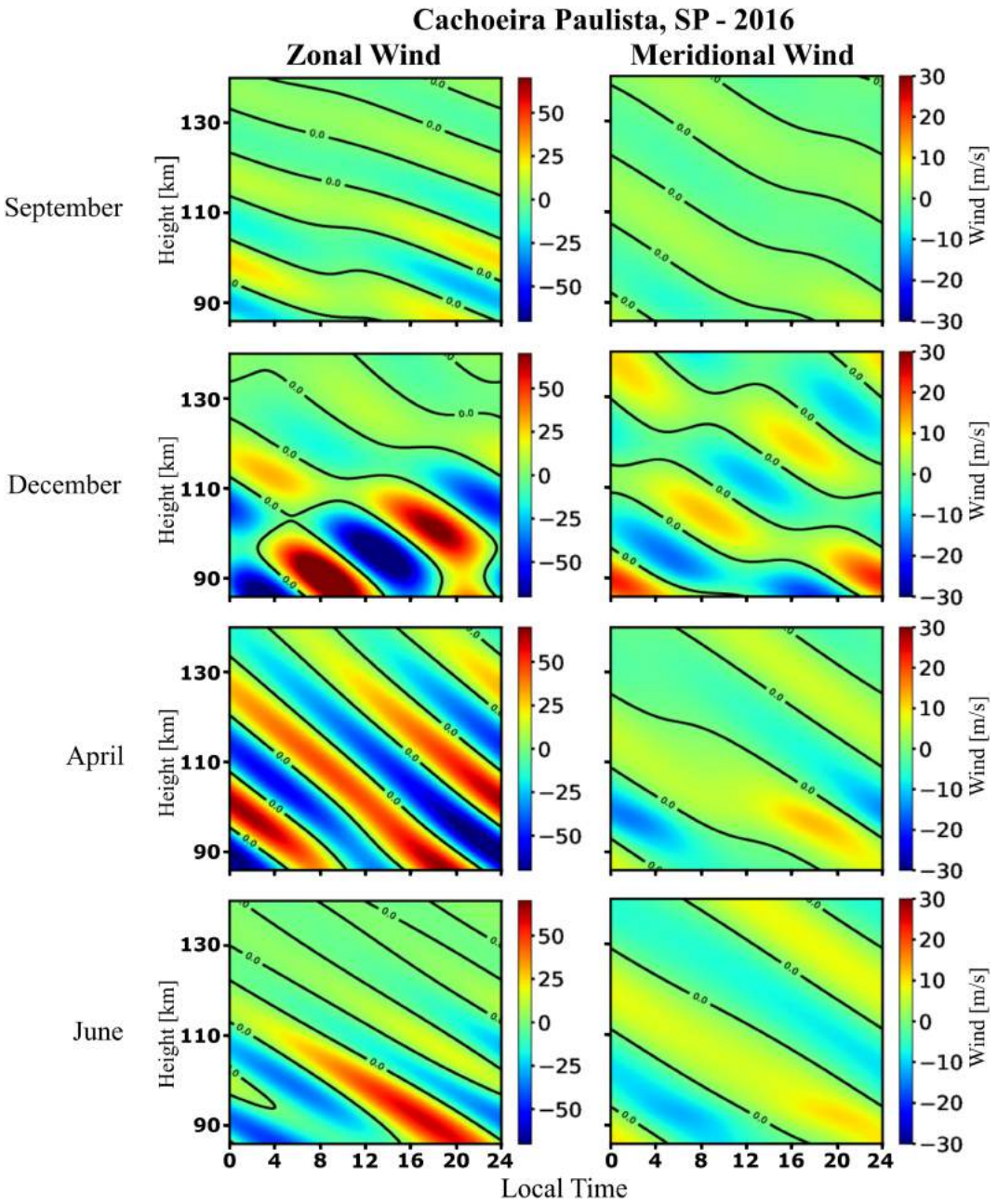

Figure 5. Profiles of the zonal and meridional winds at Cachoeira Paulista in the months of September, December, April, and June of 2016, whose data were used as input in the MIRE model to simulate *Es* layers over JAT and SJC.

layer at 00:00 LT (initially located at ~123 km) performed a downward movement until to attain ~109 km at 09:00 LT, while the lower *Es* layer (initially located at ~104 km) have decayed until to disappear. Similar behavior was observed for the highest *Es* layer at 09:00 LT that descended until ~116 km at 16:00 LT. This altitude descent of the *Es* layer is in accordance with the well-known wind shear mechanism associated with tidal winds and can be explained by the action of the diurnal, semidiurnal, and terdiurnal periodicities of the winds existing in the *E* region (Bishop & Earle, 2003; Haldoupis, 2011).

The *Es* layer electron density profiles were obtained from MIRE for the 4 months analyzed in order to compare the simulations with the ionosonde observations. In fact, the maximum electron density of the simulated *Es* layers was compared with the electron density derived from the scaled *fb*Es parameter. We have chosen the *fb*Es since this parameter is the one that better represents the electron density of the *Es* layers

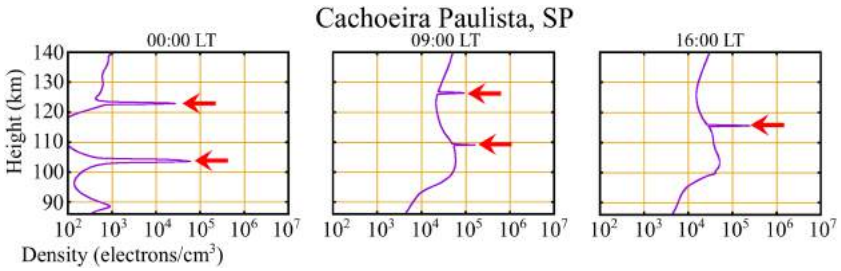

Figure 6. Examples of electron density profile (in log scale) as function of height as calculated by MIRE at 00:00, 09:00, and 16:00 LT in Cachoeira Paulista after the inclusion into the model of the zonal and meridional wind data. The case analyzed occurred in the month of June. The red arrows denote the peaks of electron density at *Es* layer heights.

(Reddy & Rao, 1968). Therefore, as mentioned before, the *fb*Es parameter is obtained where the frequency of the upper layer starts to be observed in the ionograms. The values of electron density (n_e) were calculated using the expression based on the relationship of $n_e = 1.24 \times 10^4$ (*fb*Es)^2 in electrons/cm^3, where *fb*Es is given in MHz. The comparison between the simulated and measured diurnal variations of electron density over the stations of JAT and SJC, during the 4 months, is shown in Figure 7. In the panels, the mass plots represent the *Es* electron density calculated from the *fb*Es parameter scaled from the ionograms of JAT (red dots) and SJC (blue dots). The black line for each month denotes the mean electron density determined from runs of MIRE model. The modeled electron densities shown in the left panels were generated considering as input the neutral wind profiles presented in Figure 5. Otherwise, the modeled electron densities shown in the right panels were generated considering an adjustment in the amplitude of the zonal and/or meridional wind components (Figures 8 and 9). The modifications in the neutral winds were performed in order to bring the absolute values of modeled *Es* electron density and their variations closer to observations.

It is readily seen from the mass plots of Figure 7 similarities between the diurnal and hourly variations of electron density over the stations of JAT and SJC. This scenario strongly suggests that the same formation mechanism of the *Es* layer is possibly acting across the entire region. In general, the electron density behavior for all of the months and for both stations is characterized by an enhancement at around 06:00 LT during sunrise. A broad maximum of electron density, in general, occurs during the afternoon between around 14:00 and 17:00 LT, followed by a gradual decrease after sunset. Including both stations and the 4 months, the highest and lowest values of electron density were ~$10^{6.0}$ electrons/cm^3 and ~$10^{4.5}$ electrons/cm^3, respectively. These observations are in fair agreement with previous results presented by Resende et al. (2017a). The only exception seems to occur during June when the maximum densities over JAT and SJC are observed between 16:00 and 18:00 LT.

It is noticed from the mass plots of Figure 7 that during specific times and months over both stations occurred anomalous intensifications of the electron density. For example, in September, a peak of ~$10^{6.0}$ electrons/cm^3 is observed over JAT at around 21:00 LT. In addition, an intensification is observed over SJC between around 02:00 and 04:00 LT with a peak of ~$10^{5.8}$ electrons/cm^3 and a second intensification between 21:00 and 23:00 LT with ~$10^{5.7}$ electrons/cm^3. During April, the mostly marked intensification occurred over SJC at around 23:00 LT with a peak of ~$10^{6.0}$ electrons/cm^3. Such increases in electron density are associated with sudden peaks in the *fb*Es and mean that an additional ionization might be occurring at *E*-region heights. These anomalous intensifications in electron density observed during September and April owe to the fact that geomagnetically quiet and disturbed days were not separated in the mass plots of Figure 7, and such peaks are related to disturbed time periods. Although short anomalous intensifications are not observed during December, it is notable that the electron density variations seem to be more spread, mainly during daytime when it is also somewhat denser. This fact is in accordance with a basic theory about *Es* layer, which postulates that during summer (as in December here) generally occurs larger metallic particles entrance in the atmosphere due to higher meteor flux rates (Haldoupis, 2011; Haldoupis et al., 2007).

The simulation results of electron density (black lines) showed in the lefts panels of Figure 7 were obtained as described in section 4. In the top left panel of Figure 7, it is seen for September that the simulated electron density agrees with the ionosonde data for most of the period, except between around 09:00 and 15:00 LT

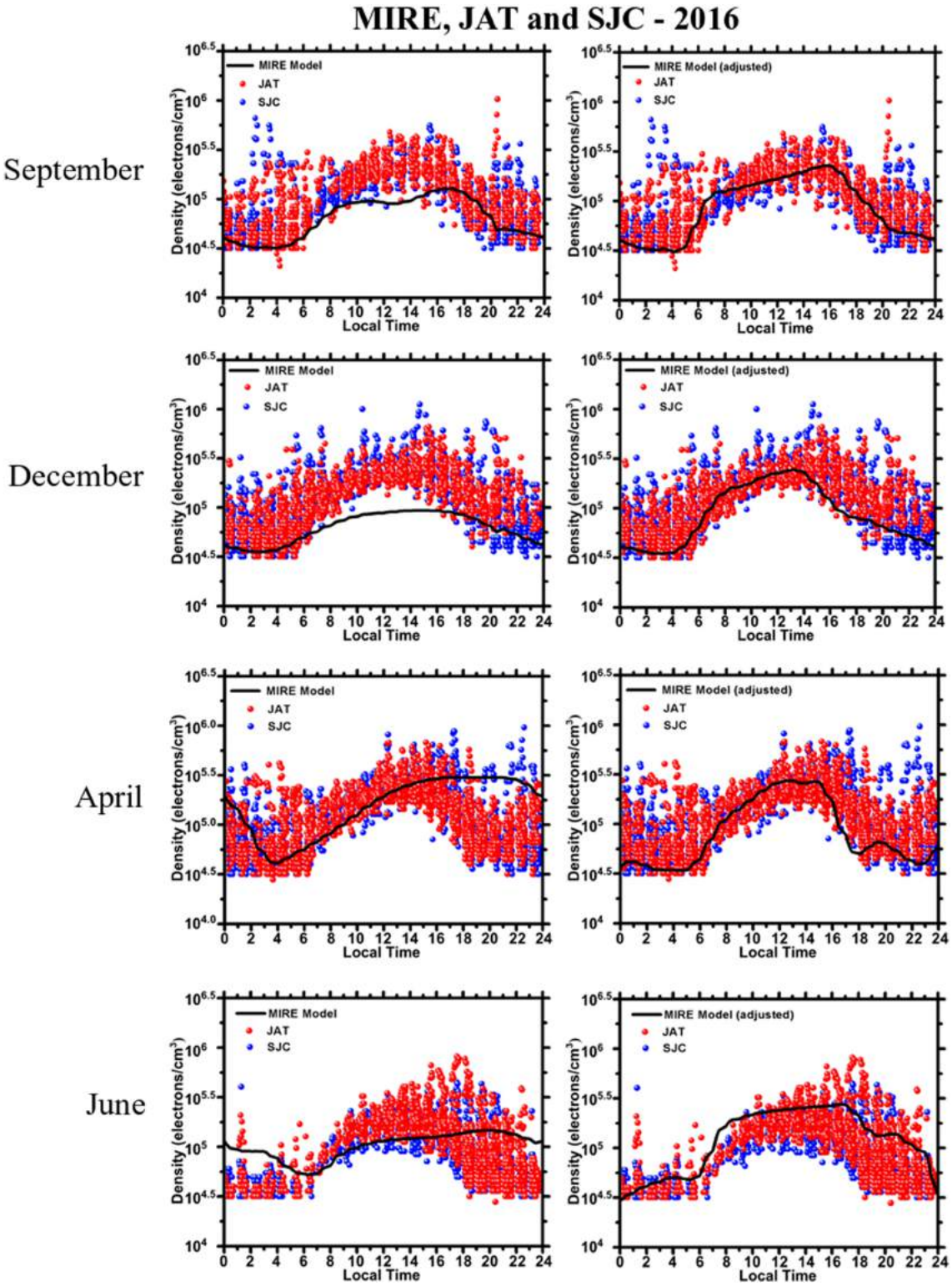

Figure 7. Mass plots of the diurnal maximum electron density variations obtained from the ionograms at JAT (red dots) and SJC (blue dots) and using the equation $n_e = 1.24x10^4 (fbEs)^2$. The comparison of the measured electron density was performed with the electron densities derived from MIRE model profiles (black lines) during September, December, April, and June (respectively from top to bottom).

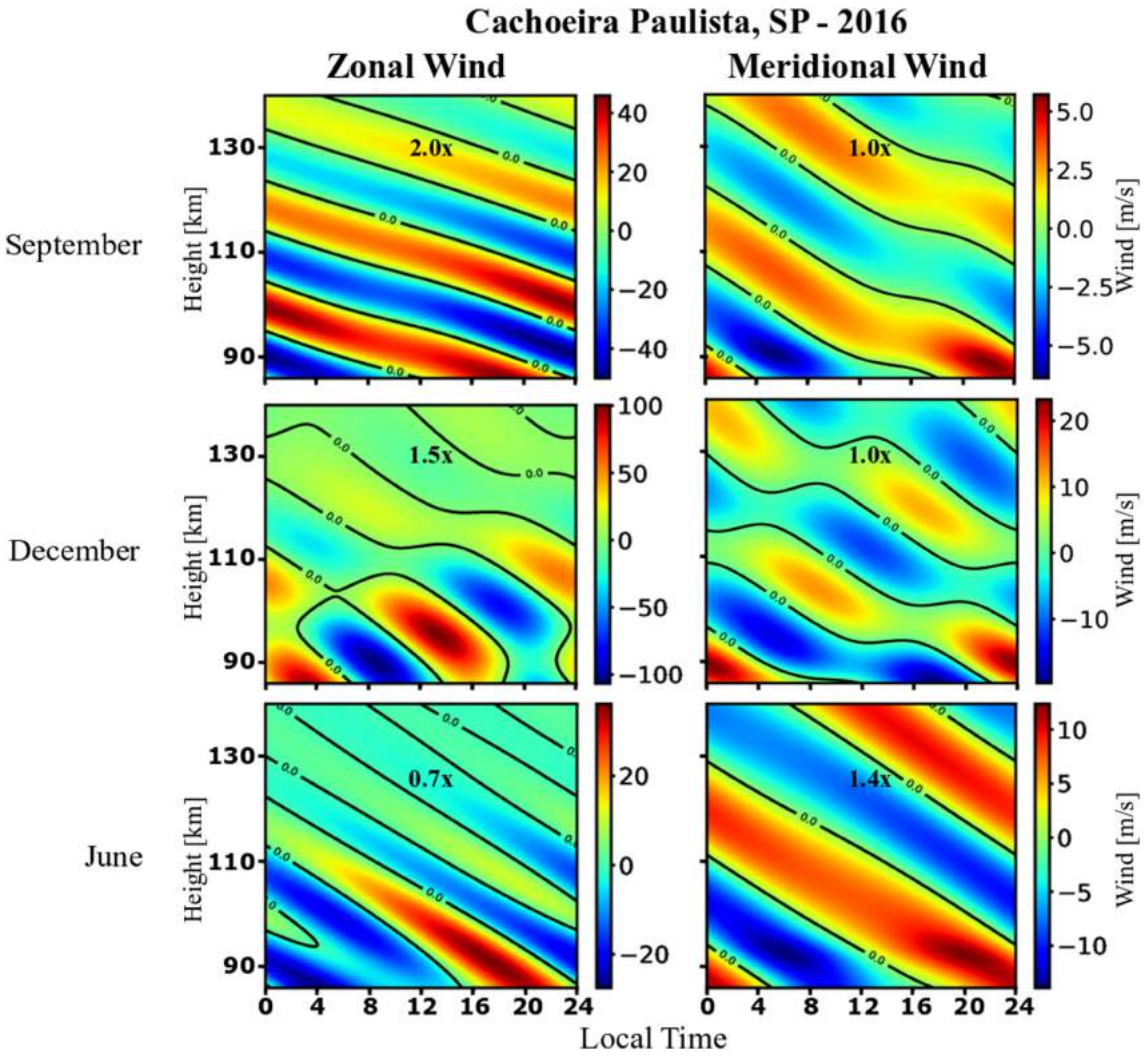

Figure 8. Profiles of the adjusted zonal and meridional wind components at Cachoeira Paulista in the months of September, December, and June of 2016, whose data were used as input in the MIRE model to better fit the *Es* layers simulated over JAT and SJC.

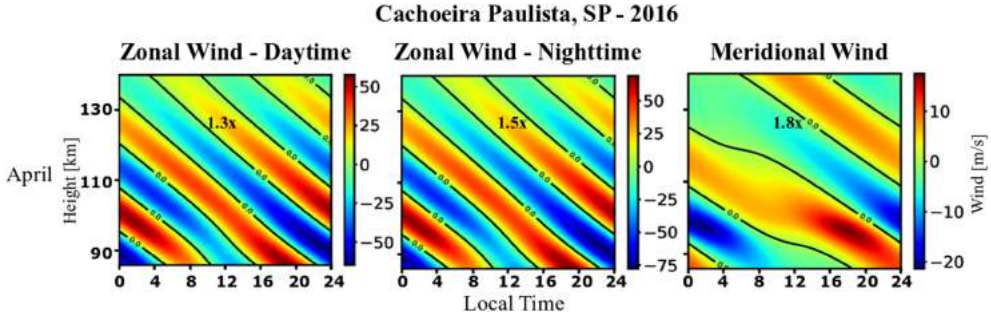

Figure 9. Profiles of the adjusted zonal and meridional wind components at Cachoeira Paulista in the month of April of 2016, whose data were used as input in the MIRE model to better fit the *Es* layers simulated over JAT and SJC. In the zonal wind daytime plot (left panel), the amplitude of the zonal component was increased by a factor of 1.3 between 06:00 and 18:00 LT. In the zonal wind nighttime plot (middle panel), the amplitude of the zonal component was increased by a factor of 1.5 between 18:00 and 06:00 LT. In the meridional wind plot (right panel), the amplitude of the meridional component was increased by a factor of 1.8 during both daytime and nighttime.

(mainly for JAT). For example, it is noticed between these times that the simulations presented maximum values of density lower than the minimum values observed from the ionosonde data, with a discrepancy of ~$10^{0.23}$ electrons/cm^3. In the simulations, the values of electron density ranged between ~$10^{4.93}$ and $10^{5.0}$ electrons/cm^3, while the minimum values of the observational data attained ~$10^{5.1}$-$10^{5.2}$ electrons/cm^3 over JAT and ~$10^{5.1}$ electrons/cm^3 over the station of SJC. However, in the top right panel of Figure 7, it is possible to see a modified form of the modeled *Es* electron density fitting better with the observations. In order to bring such absolute values of modeled electron density closer to observations, sensitive testing of the MIRE model was performed by adjusting the amplitude of the zonal and meridional wind components for all range of heights (86–140 km). In this case for September, only changes in the zonal wind were enough to produce better simulation results. The modified profile of the zonal wind component during September is now shown in the top panel of Figure 8. It is noticed that the amplitude of the zonal wind was doubled during daytime in comparison to the former estimations (Figure 5), leading the modeled electron density to ~$10^{5.1}$-$10^{5.35}$ electrons/cm^3 between 09:00 and 15:00 LT.

It is also noted in the left panel of Figure 7 for December that the most marked discrepancy occurred during the daytime between about 08:00 and 16:00 LT at both SJC and JAT, with the simulations assuming electron density values of ~$10^{0.27}$ electrons/cm^3 lower than the minimum values derived from the ionosonde data. In general, the zonal wind component is the most important to form *Es* layers at low latitudes. Thus, a possible explanation for such different behavior seen during December may be related to the very irregular zonal component of the wind shear amplitude, as noticed in Figures 5 and 8. It is possible here that the MIRE model might be underestimating the zonal wind amplitude, since interactions between tides with other types of atmospheric waves, such as gravity or planetary waves, have not been considered into the model. Moreover, it is important to note that the wind used in this model is based on the monthly mean tidal amplitude, which means the day-to-day tidal variability is also not considered. And so, this could be driving such differences between observations and modeled *Es*. By increasing the amplitude of the zonal wind during daytime by a factor of 1.5 (Figure 8), the right panel of Figure 7 for December shows a much better fitting between modeled and observed *Es* electron density. As in September, changes in the meridional wind component increased the discrepancies when tested into the model, and only modifications in the zonal wind were considered in the analysis for December.

During April and June, the left plots of Figure 7 show that the most marked discrepancy between modeled and observed electron densities occurred after about 16:00 LT up to about 03:00 LT. In terms of magnitude, the modeled density values are overestimated during April for a short period between 19:00 and 22:00 LT over JAT, while during June, it is mainly observed over SJC between about 00:00 and 03:00 LT. In these cases, the simulated electron densities were somewhat larger by ~$10^{0.25}$ electrons/cm^3. Another discrepancy observed from the results shows that the variability of electron density does not accompany the descent of the *fb*Es values after 16:00 LT. In June (right bottom panel of Figure 7), the magnitude and behavior of modeled and observed electron densities agreed better when the diurnal amplitude of the zonal wind (as shown in Figure 8) decreased by a factor of 0.7, whereas the diurnal amplitude of the meridional wind increased by a factor of 1.4. Otherwise in April, the absolute values of modeled *Es* electron density and their variations fitted better with the observations (right panel of Figure 7) when the daytime and nighttime amplitudes of the zonal wind increased, respectively, by a factor of 1.3 (left panel of Figure 9) and 1.5 (middle panel of Figure 9), whereas the diurnal amplitude of the meridional wind increased by a factor of 1.8 (right panel of Figure 9). The modifications in the amplitude of the zonal and meridional winds incorporated into the model are summarized ahead in Table 1.

Another fact that deserves to be highlighted from the simulated results (right panels of Figure 7) is the manifestation of the minimum density values between around 02:00 and 04:00 LT, mainly during September, December, and April. Around this time, the electron density simulated by MIRE reaches values close to the minimum values obtained from the ionosonde data. Resende et al. (2017a) also reported this same behavior when they compared ionosonde-derived *Es* electron densities measured during the summer of 2005 with MIRE simulations. According to them, such minimum density values of modeled *Es* occur coincidently during the times when the ionograms register the presence of the high type of sporadic layers (Es_h) with a downward movement, followed by their merging with other types of *Es* layers (e.g., Es_c or Es_l). The theory about the presence and evolution of Es_h layer is still not well established. Harper (1977) reported that the

Table 1
Daytime and Nighttime Wind Multiplicative Factors to Better Fit of the Modeled Electron Density With the Ionosonde Observations

	Zonal Wind		Meridional Wind	
Month	Daytime	Nighttime	Daytime	Nighttime
September	2.0	1.0	1.0	1.0
December	1.5	1.0	1.0	1.0
April	1.3	1.5	1.8	1.8
June	0.7	0.7	1.4	1.4

diurnal wind is more effective below 110 km to the formation of Es_h layer, whereas for higher altitudes, the main role is attributed to the semidiurnal tide. In addition, Huang and Kelley (1996) also suggested that the Es_h layers can be modulated by gravity waves. In the present study, we do not consider into MIRE the possible effects of gravity wave in the formation of *Es* layers. However, the presence of the Es_s layer, mainly during April and June over JAT and SJC, is another evidence of the possible influence of gravity waves. According to Cohen et al. (1962), the Es_s layer, although not common at low-latitude regions, once observed is an indication of the action of gravity waves in the formation/modulation of the *Es* layers. Thus, we cannot rule out that some discrepancies observed here are due to the fact that our simulations do not consider the effect of gravity waves. However, the possibility deserves further investigation in future work.

6. Conclusions

In this study, it was possible to identify in the ionograms recorded by the two observatories located inside the SAMA region (JAT and SJC), five types of *Es*-layers of the total of eight types currently existing, and registered in the U.R.S.I Handbook of Ionogram Interpretation and Reduction (Piggott & Rawer, 1972). The flat/low ($Es_{f/l}$) type of sporadic was the most frequent over both stations and during all months analyzed (April, June, September, and December of 2016), followed by the cusp (Es_c) and high (Es_h) types, whereas the slant (Es_s) type presented the lower occurrence. Over both JAT and SJC, the average rate of *Es* layers was higher during April and lower during September. The average occurrence of *Es* layers during June was larger in JAT than in SJC, whereas during December, it was the opposite. The decline in the *Es* layer occurrence during the month of September over both stations was observed to be directly related to the dramatic reduction in the occurrence of the Es_h and Es_c types. While the occurrence rate of the $Es_{f/l}$ type was significant during all months at both stations, the Es_c and Es_h types tend to be more frequent during April and December and mainly over JAT between around 10:00 and 16:00 LT. The diurnal variation of the *Es* occurrence seems to change differently for each month. For example, it may present a peak after noontime (during April in JAT) until the early evening (during June in JAT/SJC and April in SJC). In December at both stations, the larger occurrences were concentrated between midnight and the early morning. In September, the scenario was more variable at both stations, and the diurnal *Es* occurrence presented at least three peaks from morning hours to around midnight.

Additionally, during the 4 months analyzed, it was not observed the Es_a type of layer. It may be attributed to the fact that the location of the center region of maximum particle flux is not above the stations of JAT and SJC. However, the analysis of the *Es* layer frequency parameters during the moderately disturbed period of 1–5 September 2016 revealed possible evidences of energetic particle-induced *E*-layer ionization around the SAMA region associated to enhanced geomagnetic activity. The ionograms presented significant increases in the *Es* layer frequencies that suggest the enhancements of the *Es* electron densities are associated to redistribution of ionization driven by the wind shear mechanism. This analysis during storm-time periods will be investigated in more detail in a future work.

Finally, the diurnal and semidiurnal tides for the zonal and meridional wind components were considered as inputs for the MIRE model in order to verify the correlation with the ionosonde data. The *fb*Es parameter was chosen, and it has a typical behavior characterized by an enhancement during the daytime and then decreasing to low values during nighttime. Depending on local time and season, some discrepancies were found between modeled and observed *Es* electron densities. During December at SJC and JAT, the most marked discrepancy occurred between about 08:00 and 16:00 LT, with the simulations underestimating the observations. Since the zonal wind is the most important to form *Es* layers, a possible explanation for such different behavior during December may be related to the very irregular zonal component of the wind shear as observed from the zonal wind profile at ~110 km. A better fitting between MIRE results and observations was obtained when the daytime amplitude of the zonal wind used as input into the model was increased by a factor of 2.0 during September and by a factor of 1.5 during December. Otherwise in the months of April and June, the discrepancies occurred mainly during nighttime. In terms of magnitude,

the modeled electron densities were overestimated in April and June, whereas in terms of variability, the initial model results were not able to reproduce the nighttime decrease of *fb*Es. However, a better agreement between modeling and observations was obtained in April by increasing both the daytime and nighttime amplitudes of the zonal/meridional wind components. Whereas for June, the best results were obtained by decreasing (increasing) the daytime and nighttime amplitudes of the zonal (meridional) wind. It is important to mention that such discrepancies observed here between modeled and ionosonde-derived *Es* electron densities can also be attributed to the fact that our simulations do not consider the possible effects of day-to-day tidal variability, as well as their interactions with gravity and planetary waves, but the possibility also deserves further investigation in a future work.

Acknowledgments

The research is supported in part by the Coordenação de Aperfeiçoamento de Pessoal de Nível Superior—Brasil (CAPES) under the PROSUC program through Finance Code 001, the Conselho Nacional de Desenvolvimento Científico e Tecnológico (CNPq) through grants 310829/2017-8 and 199404/2017-0, and Fundação de Amparo à Pesquisa do Estado de São Paulo (FAPESP) by processes 2018/15973-8 and 2012/08445-9. L. C. A. Resende and V. F. Andrioli would like to acknowledge the China-Brazil Joint Laboratory for Space Weather (CBJLSW), National Space Science Center (NSSC), and Chinese Academy of Sciences (CAS) for supporting their postdoctoral fellowship. The ionosonde data are available for download in the link (https://www1.univap.br/ionosfera/Ionosondes_data.zip). The meteor radar data are available for download in the link (https://www1.univap.br/ionosfera/Winddata.zip). The Kp/Dst indexes are available from Geomagnetic Data Service (http://wdc.kugi.kyoto-u.ac.jp/wdc/Sec3.html). The authors thank Alan Rodger and another anonymous referee for their assistance in evaluating this paper.

References

Abdu, M. A., Batista, I. S., Carrasco, A. J., & Brum, C. G. M. (2005). South Atlantic magnetic anomaly ionization: A review and a new focus on electrodynamic effects in the equatorial ionosphere. *Journal of Atmospheric and Solar - Terrestrial Physics*, *67*, 1643–1657. https://doi.org/10.1016/j.jastp.2005.01.014

Abdu, M. A., Batista, I. S., MacDougall, J., Sobral, J. H. A., & Muralikrishna, P. (1997). Permanent changes in sporadic E layers over Fortaleza, Brazil. *Advances in Space Research*, *20*(11), 2165–2168.

Abdu, M. A., Batista, I. S., Muralikrishna, P., & Sobral, J. H. A. (1996). Long term trends in sporadic E layers and electric fields over Fortaleza, Brazil. *Geophysical Research Letters*, *23*(7), 757–760. https://doi.org/10.1029/96GL00589

Abdu, M. A., Batista, I. S., Piazza, L. R., & Massambani, O. (1981). Magnetic storm-associated enhanced particle precipitation in the South Atlantic anomaly: Evidence from VLF phase measurements. *Journal of Geophysical Research*, *86*, 7533–7542.

Andrioli, V. F., Clemesha, B. R., Batista, P. P., & Schuch, N. J. (2009). Atmospheric tides and mean winds in the meteor region over Santa Maria (29.7°S; 53.8°W). *Journal of Atmospheric and Solar - Terrestrial Physics*, *71*, 1864–1876. https://doi.org/10.1016/j.jastp.2009.07.005

Andrioli, V. F., Fritts, D. C., Batista, P. P., & Clemesha, B. R. (2013). Improved analysis of all-sky meteor radar measurements of gravity wave variances and momentum fluxes. *Annales de Geophysique*, *31*, 889–908. https://doi.org/10.5194/angeo-31-889-2013

Arras, C., Wickert, J., Beyerle, G., Heise, S., Schmidt, T., & Jacobi, C. (2008). A global climatology of ionosphericv irregularities derived from GPS radio occultation. *Geophysical Research Letters*, *35*, L14809. https://doi.org/10.1029/2008GL034158

Batista, I. S., & Abdu, M. A. (1977). Magnetic storm associated delayed sporadic-E enhancements in Brazilian geomagnetic anomaly. *Journal of Geophysical Research*, *82*, 4777–4783. https://doi.org/10.1029/JA082i029p04777

Batista, P. P., Clemesha, B. R., Tokumoto, A. S., & Lima, L. M. (2004). Structure of the mean winds and tides in the meteor region over Cachoeira Paulista, Brazil (22.7S, 45 W) and its comparison with models. *Journal of Atmospheric and Solar - Terrestrial Physics*, *66*, 623–636. https://doi.org/10.1016/j.jastp.2004.01.014

Bishop, R. L., & Earle, G. D. (2003). Metallic ion transport associated with midlatitude intermediate layer development. *Journal of Geophysical Research*, *108*(A1), 1019. https://doi.org/10.1029/2001JA009411

Carrasco, A. J. (2005). O pico pré-inversão na deriva vertical de plasma e a camada E esporádica. São José dos Campos: INPE, Brasil. [Thesis].154p. (INPE-13054-TDI/1022).

Carrasco, A. J., Batista, I. S., & Abdu, M. A. (2007). Simulation of the sporadic E layer response to prereversal associated evening vertical electric field enhancement near dip equator. *Journal of Geophysical Research*, *112*, A06324. https://doi.org/10.1029/2006JA012143

Chu, Y. H., Wang, C. Y., Wu, K. H., Chen, K. T., Tzeng, K. J., Su, C. L., et al. (2014). Morphology of sporadic E layer retrieved from COSMIC GPS radio occultation measurements: Wind shear theory examination. *Journal of Geophysical Research: Space Physics*, *119*, 2117–2136. https://doi.org/10.1002/2013JA019437

Cohen, R., Calvert, W., & Bowles, K. L. (1962). On nature of equatorial slant sporadic E. *Journal of Geophysical Research*, *67*(3), 965–972. https://doi.org/10.1029/JZ067i003p00965

Dagar, R., Verma, P., Napgal, O., & Setty, C. S. G. K. (1977). The relative effects of electric fields and neutral winds on the formation of the equatorial sporadic layers. *Annales de Geophysique*, *33*(3), 333–340.

Ferrell, O. P. (1947). Note on the sporadic E-layer. *Proceedings of the IRE*, *35*(5), 493–494.

Fytterer, T., Arras, C., Hoffmann, P., & Jacobi, C. (2014). Global distribution of the migrating terdiurnal tide seen in sporadic E occurrence frequencies obtained from GPS radio occultations. *Earth, Planets and Space*, *66*(1), 1–9. https://doi.org/10.1186/1880-5981-66-79

Haldoupis, C. (2011). Aeronomy of the Earth's Atmosphere and Ionosphere: A tutorial review of sporadic layers. Crete: University of Crete, 2011.

Haldoupis, C., Pancheva, D., Singer, W., Meek, C., & MacDougall, J. (2007). An explanation for the seasonal dependence of midlatitude sporadic E layers. *Journal of Geophysical Research*, *112*, A06315. https://doi.org/10.1029/2007JA012322

Harper, R. M. (1977). Tidal winds in 100-km to 200-km region at Arecibo. *Journal of Geophysical Research*, *82*, 3243–3250. https://doi.org/10.1029/JA082i022p03243

Helmer, M., Plane, J. M., Qian, J., & Gardner, C. S. (1998). A model of meteoric iron in the upper atmosphere. *Journal of Geophysical Research*, *103*(10), 913–925. https://doi.org/10.1029/97JD03075

Hocking, W. K., Fuller, B., & Vandepeer, B. (2001). Real-time determination of meteor-related parameters utilizing modern digital technology. *Journal of Atmospheric and Terrestrial Physics*, *63*, 155–169. https://doi.org/10.1016/S1364-6826(00)00138-3

Hocking, W. K., & Thayaparan, T. (1997). Simultaneous and colocated observation of winds and tides by MF and meteor radars over London, Canada (43 degrees N, 81 degrees W), during 1994-1996. *Radio Science*, *32*(2), 833–865. https://doi.org/10.1029/96RS03467

Huang, C.-S., & Kelley, M. C. (1996). Numerical simulations of gravity wave modulation of midlatitude sporadic E layers. *Journal of Geophysical Research*, *101*(A11), 24,533–24,543.

Lieberman, R. S., Oberheide, J., & Talaat, E. R. (2013). Nonmigrating diurnal tides observed in global thermospheric winds. *Journal of Geophysical Research: Space Physics*, *118*, 7384–7397. https://doi.org/10.1002/2013JA018975

MacDougall, J. W. (1974). 100 km neutral zonal wind patterns. *Planetary and Space Science*, *22*, 545–558.

MacDougall, J. W., Grant, I. F., & Shen, X. (1995). The Canadian advanced digital ionosonde: Design and results, Report UAG-14: Ionospheric Networks and Stations. World Data Center A for Solar-Terrestrial Physics, 21-27.

Mathews, J. D., & Bekeny, F. S. (1979). Upper atmosphere tides and the vertical motion of ionospheric sporadic layers at Arecibo. *Journal of Geophysical Research*, *84*, 2743–2750. https://doi.org/10.1029/JA084iA06p02743

Matsushita, S. (1962). Interrelations of sporadic *E* and ionospheric currents. In E. K. Smith, Jr. & S. Matsushita (Eds.), *Ionospheric sporadic E* (pp. 344–275). New York: MacMillian Company. https://doi.org/10.1016/B978-0-08-009744-2.50028-X

Nygren, T., Jalonen, L., Oksman, J., & Turunen, T. (1984). The role of electric-field and neutral wind direction in the formation of sporadic E-layers. *Journal of Atmospheric and Terrestrial Physics*, *46*(4), 373–381. https://doi.org/10.1016/0021-9169(84)90122-3

Piggott, R. W., & Rawer, K. (1972). U.R.S.I. Handbook of Ionogram Interpretation and Reduction. World Data Center A for Solar-Terrestrial Physics. Report UAG-23:NOAA, Boulder, CO.

Pillat, V. G., Guimarães, L. N. F., Fagundes, P. R., & Silva, J. D. S. (2013). A computational tool for ionosonde CADI's ionogram analysis. *Computers & Geosciences*, *52*, 372–378. https://doi.org/10.1016/j.cageo.2012.11.009

Reddy, C. A., & Rao, M. M. (1968). On the physical significance of the Es parameters fbEs, fEs and foEs. *Journal of Geophysical Research*, *73*, 331–341. https://doi.org/10.1029/JA073i017p05627

Reid, G. C. (1968). The formation of small scale irregularities in the ionosphere. *Journal of Geophysical Research*, *73*, 1627–1640. https://doi.org/10.1029/JA073i005p01627

Resende, L. C. A., Batista, I. S., Denardini, C. M., Batista, P. P., Carrasco, A. J., Andrioli, V. F., & Moro, J. (2017a). Simulations of blanketing sporadic E-layer over the Brazilian sector driven by tidal winds. *Journal of Atmospheric and Solar - Terrestrial Physics*, *154*, 104–114. https://doi.org/10.1016/j.jastp.2016.12.012

Resende, L. C. A., Batista, I. S., Denardini, C. M., Batista, P. P., Carrasco, J. A., Andrioli, V. F., & Moro, J. (2017b). The influence of tidal winds in the formation of blanketing sporadic E-layer over equatorial Brazilian region. *Journal of Atmospheric and Solar - Terrestrial Physics*, *171*, 64–71. https://doi.org/10.1016/j.jastp.2017.06.009

Resende, L. C. A., Batista, I. S., Denardini, C. M., Carrasco, A. J., Andrioli, V. F., Moro, J., et al. (2016). Competition between winds and electric fields in the formation of blanketing sporadic E layers at equatorial regions. *Earth, Planets and Space*, *68*(1), 1–14. https://doi.org/10.1186/s40623-016-0577-z

Resende, L. C. A., Denardini, C. M., & Batista, I. S. (2013). Abnormal *fbEs* enhancements in equatorial *Es* layers during magnetic storms of solar cycle 23. *Journal of Atmospheric and Solar - Terrestrial Physics*, *102*, 228–234. https://doi.org/10.1016/j.jastp.2013.05.020

Rishbeth, H., & Gariott, O. G. (1969). *Introduction to ionospheric physics* (p. 331). New York: Academic Press.

Whitehead, J. D. (1961). The formation of the sporadic-E layer in the temperate zones. *Journal of Atmospheric and Terrestrial Physics*, *20*(1), 49–58.

Whitehead, J. D. (1989). Recent work on mid-latitude and equatorial sporadic-E. *Journal of Atmospheric and Solar - Terrestrial Physics*, *51*(5), 401–424.

Yeh, W.-H., Liu, J.-Y., Huang, C.-Y., & Chen, S.-P. (2014). Explanation of the sporadic-E layer formation by comparing FORMOSAT-3/COSMIC data with meteor and wind shear information. *Journal of Geophysical Research: Atmospheres*, *119*, 4568–4579. https://doi.org/10.1002/2013JD020798